Bilayer Wigner crystals in a transition metal dichalcogenide heterostructure

https://doi.org/10.1038/s41586-021-03560-w

Received: 4 October 2020

Accepted: 15 April 2021

Published online: 30 June 2021

Check for updates

You Zhou[1,2,9], Jiho Sung[1,2], Elise Brutschea[1], Ilya Esterlis[2], Yao Wang[2,3], Giovanni Scuri[2], Ryan J. Gelly[2], Hoseok Heo[1,2], Takashi Taniguchi[4], Kenji Watanabe[5], Gergely Zaránd[6], Mikhail D. Lukin[2], Philip Kim[2,7], Eugene Demler[2,8]✉ & Hongkun Park[1,2]✉

One of the first theoretically predicted manifestations of strong interactions in many-electron systems was the Wigner crystal[1–3], in which electrons crystallize into a regular lattice. The crystal can melt via either thermal or quantum fluctuations[4]. Quantum melting of the Wigner crystal is predicted to produce exotic intermediate phases[5,6] and quantum magnetism[7,8] because of the intricate interplay of Coulomb interactions and kinetic energy. However, studying two-dimensional Wigner crystals in the quantum regime has often required a strong magnetic field[9–11] or a moiré superlattice potential[12–15], thus limiting access to the full phase diagram of the interacting electron liquid. Here we report the observation of bilayer Wigner crystals without magnetic fields or moiré potentials in an atomically thin transition metal dichalcogenide heterostructure, which consists of two MoSe$_2$ monolayers separated by hexagonal boron nitride. We observe optical signatures of robust correlated insulating states at symmetric (1:1) and asymmetric (3:1, 4:1 and 7:1) electron doping of the two MoSe$_2$ layers at cryogenic temperatures. We attribute these features to bilayer Wigner crystals composed of two interlocked commensurate triangular electron lattices, stabilized by inter-layer interaction[16]. The Wigner crystal phases are remarkably stable, and undergo quantum and thermal melting transitions at electron densities of up to 6×10^{12} per square centimetre and at temperatures of up to about 40 kelvin. Our results demonstrate that an atomically thin heterostructure is a highly tunable platform for realizing many-body electronic states and probing their liquid–solid and magnetic quantum phase transitions[4–8,17].

A Wigner crystal forms when the Coulomb interaction between electrons dominates their kinetic energy[1]. To date, the realization of quantum Wigner crystals has often relied on placing a semiconductor quantum well in a strong magnetic field[9–11]. Unlike Wigner's original picture[1], however, the application of a strong magnetic field quenches the electron kinetic energy, altering the competition between the electron kinetic energy and interaction energy and strongly favouring full spin polarization of electrons. Although hints of Wigner crystals under zero magnetic field were detected in GaAs (ref. [18]) and AlAs systems (ref. [19]), unambiguous experimental demonstrations of zero-field quantum Wigner crystals have remained a major challenge.

Recent advances in materials growth and heterostructure fabrication have enabled the preparation of high-quality heterostructures made of transition metal dichalcogenide (TMD) monolayers[20,21]. The large effective masses of charge carriers[22,23] and weak Coulomb screening in TMDs suppress the Fermi energy and enhance electron interactions, facilitating the realization of correlated electronic phases at much higher electron density[12–15,24,25] than in other semiconductors such as GaAs (refs. [9–11,18,19]). Furthermore, owing to their strong excitonic response that is sensitive to the spin and charge states, the electrical properties of TMD heterostructures can be optically probed[20,21,24–26]. Indeed, TMD heterostructures with moiré superlattices have been used to realize correlated electron solids[12–15], sometimes called generalized Wigner crystals[27], aided by the underlying moiré potential at particular electron fillings. Compared with Wigner's original picture, in which the symmetry breaking is continuous, the generalized Wigner crystals break only discrete symmetry and thus exhibit distinct phase transition behaviours.

Charge density control in MoSe$_2$ bilayers

In this work, we create MoSe$_2$ bilayer heterostructures and optically investigate the formation of bilayer Wigner crystals at zero magnetic field and high electron densities. The heterostructure device D1 consists

---

[1]Department of Chemistry and Chemical Biology, Harvard University, Cambridge, MA, USA. [2]Department of Physics, Harvard University, Cambridge, MA, USA. [3]Department of Physics and Astronomy, Clemson University, Clemson, SC, USA. [4]International Center for Materials Nanoarchitectonics, National Institute for Materials Science, Tsukuba, Japan. [5]Research Center for Functional Materials, National Institute for Materials Science, Tsukuba, Japan. [6]MTA-BME Quantum Dynamics and Correlations Research Group, Institute of Physics, Budapest University of Technology and Economics, Budapest, Hungary. [7]John A. Paulson School of Engineering and Applied Sciences, Harvard University, Cambridge, MA, USA. [8]Institute for Theoretical Physics, ETH Zürich, Zürich, Switzerland. [9]Present address: Department of Materials Science and Engineering, University of Maryland, College Park, MD, USA. ✉e-mail: demler@physics.harvard.edu; Hongkun_Park@harvard.edu

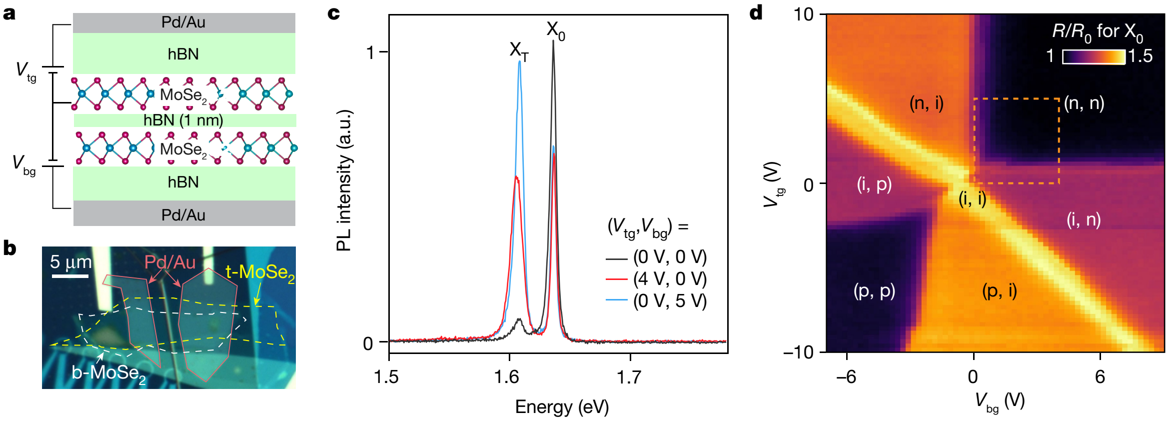

Fig. 1 | Device structure and full control of carrier density in device D1. **a**, A schematic of the heterostructure cross-section. The two MoSe$_2$ monolayers are separated by a 1-nm-thick layer of hBN. The MoSe$_2$/hBN/MoSe$_2$ structure is then encapsulated in hBN flakes of 15–20 nm thickness. **b**, An optical image of a MoSe$_2$/hBN/MoSe$_2$ device. The top and bottom MoSe$_2$ monolayer regions (t-MoSe$_2$ and b-MoSe$_2$, respectively) are indicated by the yellow and white dashed lines, respectively. The solid red lines show the outline of the optically transparent, thin, top Pd/Au gates. **c**, Representative PL spectra of the MoSe$_2$/hBN/MoSe$_2$ device measured at 4 K under different gate configurations. X_0 and X_T denote neutral and charged exciton, respectively. **d**, A 2D map of reflectance contrast (colour scale) from the neutral exciton X_0 as a function of top (V_{tg}) and bottom (V_{bg}) gate voltages at 4 K. We normalize the reflectance R to its value at the highly doped regime, R_0. From the strength of the reflectance, we can extract the charge states of the bilayer system. Here we denote the charge state as p, i or n (representing hole-doped, neutral or electron-doped, respectively), and give it in parentheses in the order top, bottom. The curved boundaries of the (p, p) region are due to Schottky contacts to p-type MoSe$_2$ with large contact resistance. The dashed box represents the voltage range we focus on in studies below.

of two MoSe$_2$ monolayers (with a nominal 0° twist angle) separated by a 1-nm-thick hexagonal boron nitride (hBN) layer (Fig. 1a, b, Methods). The carrier density in each MoSe$_2$ layer can be independently controlled by the external top-gate and bottom-gate voltages, V_{tg} and V_{bg}, through the top and bottom hBN dielectric layer. Figure 1c and Extended Data Fig. 1 show representative photoluminescence (PL) and reflectance spectra collected from the MoSe$_2$/hBN/MoSe$_2$ region under various gate configurations at temperature $T = 4$ K. Without external gating, the PL spectrum is dominated by sharp neutral intra-layer exciton (X_0) emission, accompanied by much weaker charged exciton (X_T) emission. This behaviour is similar to that of high-quality intrinsic monolayers[28], indicating that both MoSe$_2$ layers maintain their direct bandgap (Extended Data Fig. 1). Neither PL nor absorption spectra (Fig. 1c, Extended Data Fig. 1) show features attributed to inter-layer excitons, consistent with the small electric field between MoSe$_2$ layers and the relatively large inter-layer separation[25,29].

By doping one layer selectively while keeping the other intrinsic, we find that the neutral excitons in the two layers are nearly degenerate in energy (Fig. 1c). Moreover, device D1 exhibits small spatial variation of the exciton energy (about 1 meV, much smaller than the exciton

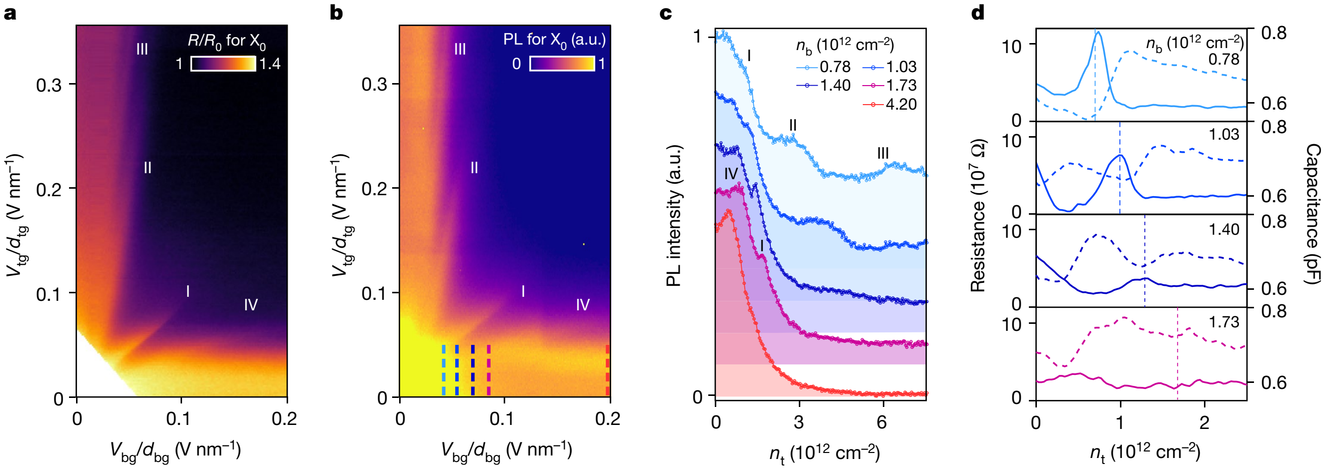

Fig. 2 | Voltage-dependent reflectance and PL spectra of device D1 in the electron-doped regime at 4 K. **a**, **b**, 2D maps of neutral exciton X_0 reflectance contrast R/R_0 (**a**) and integrated X_0 PL (**b**), as a function of V_{tg}/d_{tg} and V_{bg}/d_{bg}. Here we divide the top- and bottom-gate voltages by the respective hBN thicknesses so that the slopes of the linear features correspond to the ratios of the electrostatically induced carrier densities in each layer, n_t:n_b. Features denoted as I, II, III and IV can be clearly observed in these maps. We did not plot the data in the (i, i) region in **a** to increase the contrast of the features. **c**, The integrated X_0 PL intensity as a function of n_t, while n_b is kept constant. The lower bound of the shaded region represents zero PL intensity for each curve. The corresponding bottom-gate voltages for these linecuts are indicated by the dashed lines in **b**. **d**, The resistance (solid curves) and capacitance (dashed curves) of the gated top layer, as a function of n_t, while n_b is kept constant. These values were measured using an optically detected resistance and capacitance technique. The enhancement in resistance and reduction in capacitance are observed near where n_t equals n_b (vertical dashed lines) for an electron density of up to approximately 1.4×10^{12} cm^{-2} (see details in Extended Data Fig. 6).

linewidth) across the entire gated bilayer region (Extended Data Fig. 1). These behaviours are different from those in previous studies[25], in which excitons in the two $MoSe_2$ layers had different energies due to stochastic strain built up during sample fabrication. Such strain can cause local variations in bandgap energy and charge puddles, which can be detrimental to Wigner crystal formation.

We characterize the gate-dependent charge states of the system by measuring the reflectance of X_0, which is sensitive to the free carrier concentration[20,21,24–26] in $MoSe_2$ (Fig. 1d, Extended Data Figs. 2, 3). Along the line of $V_{tg} = -\alpha V_{bg}$ ($\alpha = d_{tg}/d_{bg}$, where d_{tg} (d_{bg}) is the top (bottom) hBN thickness), we observe strong X_0 reflectance, indicating that both $MoSe_2$ layers are intrinsic ((*i*, *i*) in Fig. 1d). When V_{tg} and V_{bg} are of the same polarity, both $MoSe_2$ layers are doped, and the reflectance is minimized.

Unexpected insulating states

The charge stability map in Fig. 1d demonstrates full control over the carrier densities in each $MoSe_2$ layer. Such precise control enables the detailed interrogation of the electronic phases as a function of charge density. We focus on the (*n*, *n*) region, where both $MoSe_2$ layers are electron-doped (the dashed box in Fig. 1d). Remarkably, we observe several strong X_0 reflectance and PL features at 4 K, denoted as I, II, III and IV, which exist at particular V_{tg}/V_{bg} ratios and diminish at higher voltages (Fig. 2a, b). Along these features, we also observe narrower X_0 linewidths and reduced X_T emission (Extended Data Figs. 1–3, Supplementary Fig. 1). Measurements of D1 at lower temperatures ($T < 1$ K) show yet another feature, V, appearing between I and II (Extended Data Fig. 4). Similar behaviour is observed in another $MoSe_2$/hBN/$MoSe_2$ device, D2, which has a 1.6-nm-thick hBN layer between two $MoSe_2$ layers (Extended Data Fig. 5).

From the PL data and a capacitance model (see Methods for the carrier density estimation based on two independent approaches), we find that features I, II, III and IV correspond to top-layer and bottom-layer electron filling ratios of $n_t{:}n_b = (1.0 \pm 0.2){:}1$, $(4.3 \pm 0.4){:}1$, $(7.4 \pm 0.7){:}1$ and $1{:}(4.0 \pm 0.4)$, respectively, where n_t (n_b) represents the electron density in the top (bottom) layer. The feature V observed at $T < 1$ K (Extended Data Fig. 4) corresponds to $n_t{:}n_b = (3 \pm 0.4){:}1$. In Fig. 2c we plot the integrated X_0 PL intensity measured at 4 K as a function of n_t for different n_b values. We observe multiple prominent peaks, corresponding to the features in Fig. 2b, the positions of which shift with varying n_b. This is in stark contrast to the situation for large n_b (for example, $4.2 \times 10^{12}\ \mathrm{cm}^{-2}$ in Fig. 2c) or for monolayers, in which the X_0 PL intensity decreases monotonically with increasing doping.

Because the reflectance and PL from X_0 depend sensitively on the presence of free carriers in the system[20,21,24–26], the increased intensity of X_0 indicates that unexpected insulating states are formed at these specific density ratios, even though both layers are electron-doped. Optically detected resistance and capacitance measurements[12] further corroborate the formation of insulating states: as shown in Fig. 2d and Extended Data Fig. 6, we find enhanced resistance along the $n_t{:}n_b = 1$ density ratio.

Density and temperature dependence

To disentangle the density-dependent behaviour of the insulating states from the intrinsic gate dependence of $MoSe_2$ monolayers[20,21,26] (Extended Data Fig. 7), we introduce a dimensionless parameter $\delta(n_t, n_b)$ that characterizes the inter-layer coupling:

$$\delta(n_t, n_b) \equiv [I_0(n_t, n_b) - I_t(n_t) - I_b(n_b)]/I_0(0,\ 0) \qquad (1)$$

Here $I_0(n_t, n_b)$ is the device's total PL intensity from X_0, and $I_t(n_t)$ ($I_b(n_b)$) is the PL intensity of X_0 from only the top (bottom) layer when its electron density is n_t (n_b). When there is no interaction between the two layers, $\delta(n_t, n_b)$ should be zero, and the value of $\delta(n_t, n_b)$ therefore quantifies the inter-layer interactions.

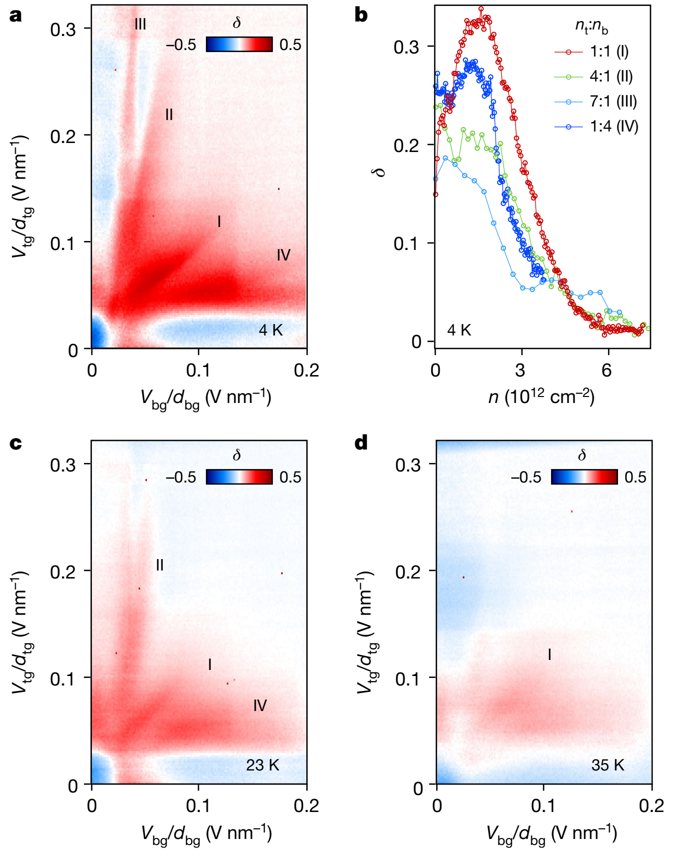

Fig. 3 | Density and temperature dependence of the interaction-induced insulating states in device D1. a, A 2D map of $\delta(n_t, n_b)$, which characterizes the formation of the interaction-induced insulating states, as a function of V_{tg}/d_{tg} and V_{bg}/d_{bg} at 4 K. **b**, δ as a function of the total electron density in both layers, $n = n_t + n_b$, for various features, that is, $n_t{:}n_b$ = 1:1, 4:1, 7:1 and 1:4 at 4 K. The density is calculated from the difference between gate voltage and threshold voltage. **c**, **d**, 2D maps of $\delta(n_t, n_b)$ as a function of V_{tg}/d_{tg} and V_{bg}/d_{bg} at 23 K (**c**) and at 35 K (**d**). (See Supplementary Fig. 4 for additional temperatures.) The negative values of δ close to zero V_{tg} or V_{bg} (below onset voltage) are due to the limitation of our method in treating intrinsic $MoSe_2$, which can have complex gate dependence due to in-gap states and weak screening. The density is calculated from the difference between gate voltage and onset voltage at which the Fermi level reaches the edge of the conduction band (Extended Data Fig. 7).

A two-dimensional (2D) map of $\delta(n_t, n_b)$ in Fig. 3a clearly shows the enhancement of δ along the particular filling ratios $n_t{:}n_b$ compared with other values. Figure 3b shows δ as a function of total electron density measured along features I–IV, that is, $n_t{:}n_b$ = 1:1, 4:1, 7:1 and 1:4. The values of δ reach their maximum at around $10^{12}\ \mathrm{cm}^{-2}$ and diminish to zero at higher densities.

Next, we characterize the temperature dependence of these insulating states. Figure 3c, d shows the 2D maps of $\delta(n_t, n_b)$ at 23 K and 35 K, respectively; the optical signatures of these insulating features are weaker than those found at 4 K (see also Extended Data Fig. 8). From these temperature-dependence studies, we find that the 1:1, 4:1 and 7:1 features exhibit different thermodynamic stabilities, and persist up to 40 K, 30 K and 23 K, respectively.

Bilayer Wigner crystals

We attribute the unexpected insulating states to bilayer Wigner crystals (Fig. 4a). As discussed, the large effective masses of carriers[22,23] and weak Coulomb screening in a TMD heterostructure are conducive to Wigner crystal formation. Furthermore, theoretical studies have predicted that the inter-layer Coulomb interactions stabilize a bilayer Wigner crystal

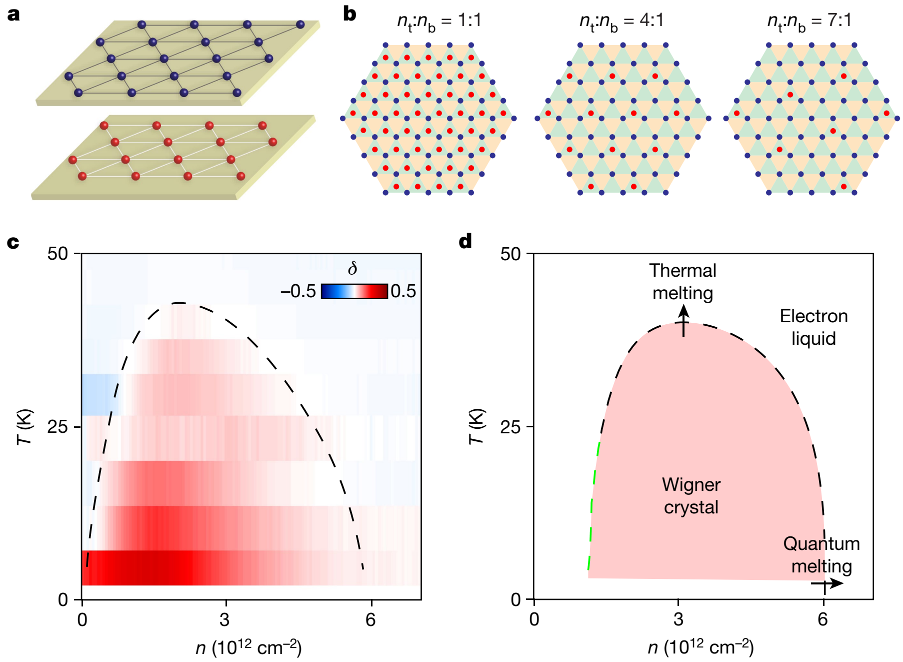

Fig. 4 | Bilayer Wigner crystals and their quantum and thermal phase transitions. a, A schematic of Wigner crystals in bilayer systems. **b**, Schematics of commensurate stacking in bilayer Wigner crystals with triangular lattices for filling ratios n_t:n_b of 1:1, 4:1 and 7:1. **c**, A 2D map of $\delta(n_t, n_b)$ as a function of total carrier density n and temperature T for n_t:n_b = 1:1. The $\delta > 0$ region represents where the bilayer Wigner crystal forms (the $\delta = 0$ boundary is shown as a dashed line). The centre position of each pixel in the y direction represents the temperature. **d**, A schematic phase diagram of bilayer Wigner crystals, showing both quantum and thermal phase transitions. The dashed line (both green and black parts) represents a calculated melting curve assuming a Lindemann parameter $\gamma \approx 0.56$. Below a density of about 1.4×10^{12} cm^{-2} (green part of the dashed line), theory predicts that the staggered triangular lattice structure becomes unstable, giving way to a sequence of structural transitions[34,46] (Supplementary Fig. 5).

phase relative to two uncoupled single-layer Wigner crystals[16]. Unlike generalized Wigner crystals in moiré superlattices that exist only at particular fillings[12–15], the bilayer Wigner crystals observed in our system are stable for a continuous range of total density with a fixed doping ratio of top and bottom layers.

To understand the formation of bilayer Wigner crystals, we consider a model in which the inter-layer interaction is treated as a perturbation to two monolayer Wigner crystals and the stable bilayer lattices form only at particular n_t:n_b values at which two triangular lattices form commensurate stacking (Fig. 4). Geometrical considerations dictate that the first few n_t:n_b to form commensurate lattices are 1:1, 3:1, 4:1 and 7:1 (Fig. 4b; see Supplementary Information for details), consistent with our experimental observation. Given that a typical inter-electron separation is about 6 nm at $n \approx 1 \times 10^{12}$ cm^{-2} and a suitable inter-layer separation (considering the thickness of MoSe$_2$) is 1.6 nm, the observation that this simple 'weak-coupling' model matches our experimental data is surprising. However, previous studies have shown that the highly anisotropic dielectric constants of hBN (ref. [30]) and non-local screening effects[31] can substantially reduce inter-layer Coulomb interactions relative to intra-layer interactions (see Supplementary Information for discussions), providing a possible rationale for the weak-coupling scenario. We note that these simple considerations do not explain why the 3:1 feature appears at a lower temperature than the 1:1, 4:1 and 7:1 features in device D1 (Extended Data Fig. 4). This observation suggests that the thermodynamic stability of each lattice may depend on other extrinsic factors (for example, disorder, lattice strain or reconstruction), which requires further study. In addition to insulating states appearing at specific density ratios, the umklapp resonances, which have recently been identified as another signature of Wigner crystals[32], are also observed from D1 (see Extended Data Fig. 10).

The density and temperature dependences of the insulating states, as inferred from Figs. 2 and 3, provide insight into the nature of the quantum and thermal melting of the Wigner crystal. With increasing electron density, the kinetic energy of the electrons increases faster than the potential energy, eventually melting the Wigner crystal. Notably, at 4 K, the Fermi energy (E_F) of the electrons near the critical density ($E_F \approx 10$ meV (refs. [22,23]) near n_t (or n_b) of 3×10^{12} cm^{-2}) is much larger than the thermal energy ($k_BT \approx 0.3$ meV), and thus the system exhibits a quantum melting behaviour. This transition occurs at $r_s \approx 11$, where r_s is the interaction parameter, defined as the ratio of Coulomb to Fermi energies (see Methods)[4].

Phase diagram

Figure 4c shows a 2D map of $\delta(n_t, n_b)$ for n_t:n_b = 1:1 as a function of n and T. Taking $\delta > 0$ as a proxy for the interaction-driven insulating state, the phase boundary between an electron solid and a liquid can be approximated by the $\delta = 0$ line (dashed line in Fig. 4c). This experimentally extracted phase boundary resembles the generic theoretical phase diagram of a Wigner crystal[33] that exhibits the quantum and thermal phase transitions.

To obtain a qualitative understanding of the bilayer Wigner crystal phase diagram, we calculate the phonon spectrum for the classical bilayer Wigner crystal and estimate the melting curve via a modified Lindemann criterion appropriate to two dimensions[4,34]. Specifically, we assume that melting occurs when the ratio between the root-mean-square fluctuations of the nearest-neighbour electron distance and the lattice constant exceeds a critical value (the Lindemann parameter γ: see Supplementary Information for details). Here we focus on the ratio 1:1. Previous studies have found that the γ value for the bilayer crystal is dependent on the inter-layer separation[35]. We therefore treat it as a fitting parameter. Matching to the $T = 4$ K critical density, we find $\gamma \approx 0.56$. We contrast this with the monolayer Wigner crystal, in which numerical simulations[4,36] have shown $\gamma \approx 0.1–0.3$. The large value of γ in our system, which is a direct reflection of the high critical density observed in the experiment, indicates the enhanced stability of the bilayer crystal. As shown in Fig. 4d, a melting curve calculated with a modified Lindemann criterion tracks the experimentally determined $\delta(n_t, n_b)$ map in Fig. 4c well (see also Extended Data Fig. 9). While the fitting procedure described here yields a melting curve compatible with experimental data, further experimental and theoretical work is needed to understand the mechanism of the dramatic enhancement of stability of the bilayer crystal.

We note that the critical density and temperature scales for melting in Fig. 4c are most likely to be overestimates of the true values. Indeed, the $\delta = 0$ line in Fig. 4c is more precisely understood as a crossover to the insulating regime, which would precede the establishment of long-range order. The robustness of insulating states for specific n_t:n_b values nevertheless suggests that even in the presence of disorder[37], the Wigner crystal domains are still sufficiently large to establish local crystalline order. Further optical and transport studies are required to interrogate the interplay between the crystalline correlations and disorder in greater detail[6,38,39].

Discussion and outlook

Our observations of bilayer Wigner crystals in atomically thin semiconductor heterostructures without a magnetic field or moiré potential open up new avenues for creating and manipulating these collective quantum phases of electrons[6,38–40]. With electrically tunable carrier density and coupling strength, these devices should enable studies of quantum and classical phase transitions in engineered many-body correlated systems[40]. Wigner crystals based on other atomically thin TMDs may also enable, for instance, the study of Wigner crystallization of holes with large spin–orbit coupling. Unlike a single-layer Wigner crystal, which has only one stable lattice structure, bilayer Wigner crystals exhibit a rich structural phase diagram depending on their filling ratios and coupling strength (Supplementary Figs. 5, 6), and possess unique collective modes such as optical phonons[34,41]. They can be controlled and probed both optically and electrically, and may be readily integrated with functional substrates to create on-chip devices for quantum simulations[42,43]. One intriguing possibility involves the realization and exploration of tunable spin Hamiltonians that could be used for creating exotic spin states[42,43], opening up new ways to simulate and manipulate spin dynamics in various lattice geometries[44,45].

Online content

Any methods, additional references, Nature Research reporting summaries, source data, extended data, supplementary information, acknowledgements, peer review information; details of author contributions and competing interests; and statements of data and code availability are available at https://doi.org/10.1038/s41586-021-03560-w.

1. Wigner, E. On the interaction of electrons in metals. *Phys. Rev*. **46**, 1002–1011 (1934).
2. Grimes, C. C. & Adams, G. Evidence for a liquid-to-crystal phase transition in a classical, two-dimensional sheet of electrons. *Phys. Rev. Lett*. **42**, 795–798 (1979).
3. Shapir, I. et al. Imaging the electronic Wigner crystal in one dimension. *Science* **364**, 870–875 (2019).
4. Monarkha, Y. P. & Syvokon, V. E. A two-dimensional Wigner crystal (Review Article). *Low Temp. Phys*. **38**, 1067–1095 (2012).
5. Spivak, B. & Kivelson, S. A. Phases intermediate between a two-dimensional electron liquid and Wigner crystal. *Phys. Rev. B* **70**, 155114 (2004).
6. Spivak, B., Kravchenko, S. V., Kivelson, S. A. & Gao, X. P. A. Colloquium: Transport in strongly correlated two dimensional electron fluids. *Rev. Mod. Phys*. **82**, 1743–1766 (2010).
7. Ortiz, G., Harris, M. & Ballone, P. Zero temperature phases of the electron gas. *Phys. Rev. Lett*. **82**, 5317 (1999).
8. Chakravarty, S., Kivelson, S., Nayak, C. & Voelker, K. Wigner glass, spin liquids and the metal-insulator transition. *Phil. Mag. B* **79**, 859–868 (1999).
9. Andrei, E. Y. et al. Observation of a magnetically induced Wigner solid. *Phys. Rev. Lett*. **60**, 2765–2768 (1988).
10. Jiang, H. W. et al. Quantum liquid versus electron solid around $\nu = 1/5$ Landau-level filling. *Phys. Rev. Lett*. **65**, 633–636 (1990).
11. Ma, M. K. et al. Thermal and quantum melting phase diagrams for a magnetic-field-induced Wigner solid. *Phys. Rev. Lett*. **125**, 036601 (2020).
12. Regan, E. C. et al. Mott and generalized Wigner crystal states in WSe$_2$/WS$_2$ moiré superlattices. *Nature* **579**, 359–363 (2020).
13. Xu, Y. et al. Correlated insulating states at fractional fillings of moiré superlattices. *Nature* **587**, 214–218 (2020).
14. Huang, X. et al. Correlated insulating states at fractional fillings of the WS$_2$/WSe$_2$ moiré lattice. *Nat. Phys*. **17**, 715–719 (2021).
15. Jin, C. et al. Stripe phases in WSe$_2$/WS$_2$ moiré superlattices. *Nat. Mater*. https://doi.org/10.1038/s41563-021-00959-8 (2021).
16. Świerkowski, L., Neilson, D. & Szymański, J. Enhancement of Wigner crystallization in multiple-quantum-well structures. *Phys. Rev. Lett*. **67**, 240 (1991).
17. Benenti, G., Waintal, X. & Pichard, J.-L. New quantum phase between the Fermi glass and the Wigner crystal in two dimensions. *Phys. Rev. Lett*. **83**, 1826–1829 (1999).
18. Yoon, J., Li, C. C., Shahar, D., Tsui, D. C. & Shayegan, M. Wigner crystallization and metal-insulator transition of two-dimensional holes in GaAs at $B = 0$. *Phys. Rev. Lett*. **82**, 1744–1747 (1999).
19. Hossain, M. S. et al. Observation of spontaneous ferromagnetism in a two-dimensional electron system. *Proc. Natl Acad. Sci*. **117**, 32244–32250 (2020).
20. Scuri, G. et al. Large excitonic reflectivity of monolayer MoSe$_2$ encapsulated in hexagonal boron nitride. *Phys. Rev. Lett*. **120**, 037402 (2018).
21. Back, P., Zeytinoglu, S., Ijaz, A., Kroner, M. & Imamoğlu, A. Realization of an electrically tunable narrow-bandwidth atomically thin mirror using monolayer MoSe$_2$. *Phys. Rev. Lett*. **120**, 037401 (2018).
22. Kormányos, A. et al. k·p theory for two-dimensional transition metal dichalcogenide semiconductors. *2D Mater*. **2**, 022001 (2015).
23. Larentis, S. et al. Large effective mass and interaction-enhanced Zeeman splitting of K-valley electrons in MoSe$_2$. *Phys. Rev. B* **97**, 201407 (2018).
24. Tang, Y. et al. Simulation of Hubbard model physics in WSe$_2$/WS$_2$ moiré superlattices. *Nature* **579**, 353–358 (2020).
25. Shimazaki, Y. et al. Strongly correlated electrons and hybrid excitons in a moiré heterostructure. *Nature* **580**, 472–477 (2020).
26. Ross, J. S. et al. Electrical control of neutral and charged excitons in a monolayer semiconductor. *Nat. Commun*. **4**, 1474 (2013).
27. Hubbard, J. Generalized Wigner lattices in one dimension and some applications to tetracyanoquinodimethane (TCNQ) salts. *Phys. Rev. B* **17**, 494–505 (1978).
28. Zhou, Y. et al. Controlling excitons in an atomically thin membrane with a mirror. *Phys. Rev. Lett*. **124**, 027401 (2020).
29. Sung, J. et al. Broken mirror symmetry in excitonic response of reconstructed domains in twisted MoSe$_2$/MoSe$_2$ bilayers. *Nat. Nanotechnol*. **15**, 750–754 (2020).
30. Geick, R., Perry, C. H. & Rupprecht, G. Normal modes in hexagonal boron nitride. *Phys. Rev*. **146**, 543–547 (1966).
31. Van der Donck, M. & Peeters, F. M. Interlayer excitons in transition metal dichalcogenide heterostructures. *Phys. Rev. B* **98**, 115104 (2018).
32. Smoleński, T. et al. Observation of Wigner crystal of electrons in a monolayer semiconductor. Preprint at https://arxiv.org/abs/2010.03078 (2020).
33. Platzman, P. M. & Fukuyama, H. Phase diagram of the two-dimensional electron liquid. *Phys. Rev. B* **10**, 3150–3158 (1974).
34. Goldoni, G. & Peeters, F. M. Stability, dynamical properties, and melting of a classical bilayer Wigner crystal. *Phys. Rev. B* **53**, 4591–4603 (1996).
35. Schweigert, I. V., Schweigert, V. A. & Peeters, F. M. Enhanced stability of the square lattice of a classical bilayer Wigner crystal. *Phys. Rev. B* **60**, 14665–14674 (1999).
36. Bedanov, V. M., Gadiyak, G. V. & Lozovik, Y. E. On a modified Lindemann-like criterion for 2D melting. *Phys. Rev. A* **109**, 289–291 (1985).
37. Imry, Y. & Ma, S.-k. Random-field instability of the ordered state of continuous symmetry. *Phys. Rev. Lett*. **35**, 1399–1401 (1975).
38. Ruzin, I. M., Marianer, S. & Shklovskii, B. I. Pinning of a two-dimensional Wigner crystal by charged impurities. *Phys. Rev. B* **46**, 3999–4008 (1992).
39. Chitra, R. & Giamarchi, T. Zero field Wigner crystal. *Eur. Phys. J. B* **44**, 455–467 (2005).
40. Waintal, X. On the quantum melting of the two-dimensional Wigner crystal. *Phys. Rev. B* **73**, 075417 (2006).
41. Bonsall, L. & Maradudin, A. A. Some static and dynamical properties of a two-dimensional Wigner crystal. *Phys. Rev. B* **15**, 1959–1973 (1977).
42. Tanatar, B. & Ceperley, D. M. Ground state of the two-dimensional electron gas. *Phys. Rev. B* **39**, 5005–5016 (1989).
43. Knörzer, J. et al. Wigner crystals in two-dimensional transition-metal dichalcogenides: spin physics and readout. *Phys. Rev. B* **101**, 125101 (2020).
44. Chen, Y. P. Pinned bilayer Wigner crystals with pseudospin magnetism. *Phys. Rev. B* **73**, 115314 (2006).
45. Dayal, S., Clay, R. T., Li, H. & Mazumdar, S. Paired electron crystal: order from frustration in the quarter-filled band. *Phys. Rev. B* **83**, 245106 (2011).
46. Monarkha, Y. & Kono, K. *Two-Dimensional Coulomb Liquids and Solids* (Springer, 2004).

Publisher's note Springer Nature remains neutral with regard to jurisdictional claims in published maps and institutional affiliations.

© The Author(s), under exclusive licence to Springer Nature Limited 2021

Methods

Device fabrication

Monolayer $MoSe_2$ and hBN flakes were exfoliated from bulk crystals[47] onto silicon substrates with a 285-nm silicon oxide layer. Monolayers of $MoSe_2$ were identified under an optical microscope and verified via PL measurements. The thickness of hBN flakes was measured by an atomic force microscope. Then we fabricated the hBN/$MoSe_2$/hBN/$MoSe_2$/hBN heterostructure using a tear-and-stack technique with a dry transfer method[48]; a monolayer of $MoSe_2$ was torn into two pieces which were then stacked without introducing any rotation between them. This heterostructure was then transferred onto the bottom gate (1-nm Cr and 9-nm Pd/Au alloy), pre-patterned by electron-beam lithography and thermal evaporation. Then top gates (1-nm Cr and 9-nm Pd/Au alloy) were defined with electron-beam lithography and deposited via thermal evaporation. Finally, we made electrical contacts to the $MoSe_2$ and the gates using 5-nm Cr and 90-nm Au deposited via thermal evaporation to connect them to the wire-bonding pads.

Optical spectroscopy

Optical measurements were carried out in a home-built confocal microscope with a 4 K cryostat from Montana Instruments and a Bluefors dilution refrigerator. The apochromatic objective used has a numerical aperture of 0.75. We excited the sample using a 660-nm-wavelength diode laser for the PL measurements. The incident laser power ranges from 100 nW to 10 μW, and we did not observe a strong power dependence of the feature in this power range. We obtained the reflectance spectra by illuminating the sample with a broadband light source, using a halogen lamp (Thorlabs SLS201L) and a supercontinuum laser from NKT Photonics, with an average power of 10–100 nW. The spectra were measured by a spectrometer using either a 300 lines per mm or a 1,200 lines per mm grating and a Princeton Instruments camera (PIXIS 2048). The gate voltages were supplied by two Keithley 2400 sourcemeters.

Estimation of doping density and ratio

Since we only extract the carrier density from the region where both layers are doped with electrons, the quantum capacitance of the two layers is much larger than the geometric gate capacitances. Because the total capacitance is dominated by the smallest individual capacitance for capacitors in series, the capacitance of our device can be approximated by the geometric capacitance. Furthermore, the hBN between the two layers of $MoSe_2$ also has a negligible contribution to the total capacitance since its thickness (1 nm) is much smaller than either the top- or bottom-gate dielectric thickness (~20 nm). In this case, the electron density in both layers can be simply obtained from the parallel-plate capacitor model as $n_t = \varepsilon_0\varepsilon_{hBN}\Delta V_{tg}/d_{tg}$ and $n_b = \varepsilon_0\varepsilon_{hBN}\Delta V_{bg}/d_{bg}$, where ε_0 is the vacuum permittivity, $\varepsilon_{hBN} \approx 3.9$ is the dielectric constant of hBN (ref. [49]) d_{tg} (d_{bg}) is the thicknesses of the top (bottom) hBN gate dielectric, and ΔV_{tg} (ΔV_{bg}) is the applied top (bottom) gate voltage relative to the onset voltage corresponding to the conduction band edge (see Extended Data Fig. 7 for an example of a band edge), which can be extracted from the 2D map shown in Fig. 2. We can also estimate the density based on the blueshift of excitons[32,50] which is within 10% of the density estimated by this simple capacitance model (Supplementary Fig. 2). Because of the linear relationship between Δn and ΔV_g, the filling ratio n_t:n_b along the linear features in Fig. 2 can be extracted by n_t:$n_b = \Delta n_t/\Delta n_b = \Delta V_{tg}d_{bg}/\Delta V_{bg}d_{tg}$, which only depends on the voltage slope of the features and the thicknesses of hBN. We note that since the reflection of X_0 exhibits complex lineshapes (Extended Data Fig. 1) due to multiple interferences between the X_0 reflectance and the substrate, it is more reliable to extract $\Delta n_t/\Delta n_b$ from the integrated X_0 PL intensity. To do so, we took the second derivative of the X_0 PL intensity with respect to the electric field ($\Delta V_{tg}/d_{tg} - \Delta V_{bg}/d_{bg}$) and obtained the slope of the local minimum of the second derivative (Supplementary Fig. 3). The values obtained from directly fitting the PL data in Fig. 2 yield similar results.

Resistance from optical detection

The optically detected resistance and capacitance measurements were carried out in a home-built confocal microscope with a 4 K cryostat (Extended Data Fig. 6). We applied a d.c. voltage V_{tg} plus an additional a.c. modulation voltage, $\Delta\tilde{V}$, using a function generator. The a.c. voltage had a peak-to-peak amplitude of 30 mV with frequencies varying from 1 kHz to 10 kHz. The data in Extended Data Fig. 6 were measured with a frequency of 5.731 kHz. The bottom-gate voltage was supplied by a Keithley 2400 sourcemeter. A continuous-wave Ti:sapphire laser from M Squared was used to detect the change of excitonic reflectance due to the carrier concentration change in the top $MoSe_2$ monolayer at its neutral exciton resonance. The incident laser power ranges from 100 μW to 300 μW. The reflected light is collected with an avalanche photodiode (Thorlabs APD 430A) and its a.c. variation is analysed using a lock-in amplifier (Stanford Research SR830).

Following the effective circuit model presented in ref. [12], the optical contrast change ΔOC induced by the a.c. voltage is given by

$$\Delta \mathrm{OC} = \alpha\Delta\tilde{n} = \frac{\alpha}{A_2 e}\Delta\tilde{V}\frac{C_1}{C_1 + C_B}\frac{1}{\frac{1}{C_{\mathrm{eff}}} + i\omega R} \qquad (2)$$

with

$$\frac{1}{C_{\mathrm{eff}}} = \frac{1}{C_1 + C_B} + \frac{1}{C_2} + \frac{1}{C_Q} \qquad (3)$$

where ω is the excitation frequency, e is the electron charge, and $\alpha = \Delta\mathrm{OC}/\Delta\tilde{n}$ is the optical detection responsivity at the probed spot, which is constant for the fixed bottom-gate voltage. C_Q and R are the quantum capacitance and resistance of the region covered by the top gate, respectively. A_2 is the area of the TMD gated by the bottom gate but not covered by the top gate. C_1 and C_B are the geometric capacitances between the TMD and the top and bottom gates in the region covered by the top gate, and C_2 is the capacitance formed between the bottom gate and the part of the TMD not covered by the top gate. These capacitances can be evaluated from the single parallel plate model using the respective gate dielectric thickness, area, and the dielectric constant of hBN. The optical detection responsivity, α, can be obtained at high V_{tg}, where the quantum capacitance, C_Q, is much larger than the geometric capacitances so the effective capacitance C_{eff} is only due to contributions from the geometric capacitances. We can also estimate α based on the gate dependence of the sample reflectance for each gate voltage, which agrees with the value from large V_{tg}. Therefore, based on these values, we can extract the values of C_Q and R under specific top and bottom d.c. voltages.

Estimating the interaction parameter r_s

For characterizing quantum melting, it is conventional to introduce a dimensionless parameter r_s, the ratio of the Coulomb energy to the Fermi energy, or equivalently the ratio of the average inter-electron distance to the effective Bohr radius. For 2D systems, r_s is given by $(me^2/4\pi\hbar^2\varepsilon\varepsilon_0)/(\pi n)^{1/2}$, where m is the electron effective mass, ε is the dielectric constant and n is the electron density. We estimate a critical r_s of ~11 based on the a single layer density n of 3×10^{12} cm^{-2}, a dielectric constant ε of 4.5, and an electron effective mass of $0.8m_e$ (ref. [23]). We note that the Coulomb energy in our system deviates from the unscreened Coulomb potential at small inter-electron distance, which can change the value slightly (see Supplementary Information for additional discussion).

Data availability

The data that support the plots within this paper and other findings of this study are available from the corresponding authors upon reasonable request.

47. Cevallos, F. A. et al. Liquid salt transport growth of single crystals of the layered dichalcogenides MoS_2 and WS_2. *Cryst. Growth Des*. **19**, 5762–5767 (2019).
48. Kim, K. et al. van der Waals heterostructures with high accuracy rotational alignment. *Nano Lett*. **16**, 1989–1995 (2016).
49. Kim, K. et al. Band alignment in WSe_2–graphene heterostructures. *ACS Nano* **9**, 4527–4532 (2015).
50. Smoleński, T. et al. Interaction-induced Shubnikov–de Haas oscillations in optical conductivity of monolayer $MoSe_2$. *Phys. Rev. Lett*. **123**, 097403 (2019).

Acknowledgements We acknowledge support from the DoD Vannevar Bush Faculty Fellowship (N00014-16-1-2825 for H.P., N00014-18-1-2877 for P.K.), NSF CUA (PHY-1125846 for H.P., E.D. and M.D.L.), Samsung Electronics (for H.P. and P.K.), NSF (PHY-1506284 for H.P. and M.D.L., DGE-1745303 for E.B., DMR-2038011 for Y.W.), AFOSR MURI (FA9550-17-1-0002), ARL (W911NF1520067 for H.P. and M.D.L.), DOE (DE-SC0020115 for H.P. and M.D.L.), AFOSR (FA9550-21-1-0216 for E.D.) and BME's TKP 2020 Nanotechnology grant (G.Z.). Device fabrication was carried out at the Harvard Center for Nanoscale Systems. Y.W. acknowledges Frontera computing system at the Texas Advanced Computing Center for geometric optimization of crystal structures. I.E. and E.D. acknowledge resources of the National Energy Research Scientific Computing Center (NERSC) for phase transition calculations. NERSC is a US Department of Energy Office of Science User Facility operated under contract no. DE-AC02-05CH11231.

Author contributions H.P. and Y.Z. conceived the project. Y.Z., J.S. and E.B. fabricated the samples, and designed and performed the experiments. I.E., Y.W., G.Z. and E.D. developed the theoretical model, and Y.Z., J.S., E.B., I.E. and Y.W. analysed the data. G.S. assisted with optical measurements, G.S. and R.J.G. assisted with sample fabrication, and H.H. grew the $MoSe_2$ crystals. T.T. and K.W. provided hBN samples. Y.Z., J.S., E.B., I.E., Y.W., G.S., E.D. and H.P. wrote the manuscript with extensive input from the other authors. H.P., E.D., P.K. and M.D.L. supervised the project.

Competing interests The authors declare no competing interests.

Additional information

Supplementary information The online version contains supplementary material available at https://doi.org/10.1038/s41586-021-03560-w.

Correspondence and requests for materials should be addressed to E.D. or H.P.

Peer review information *Nature* thanks the anonymous reviewers for their contribution to the peer review of this work.

Reprints and permissions information is available at http://www.nature.com/reprints.

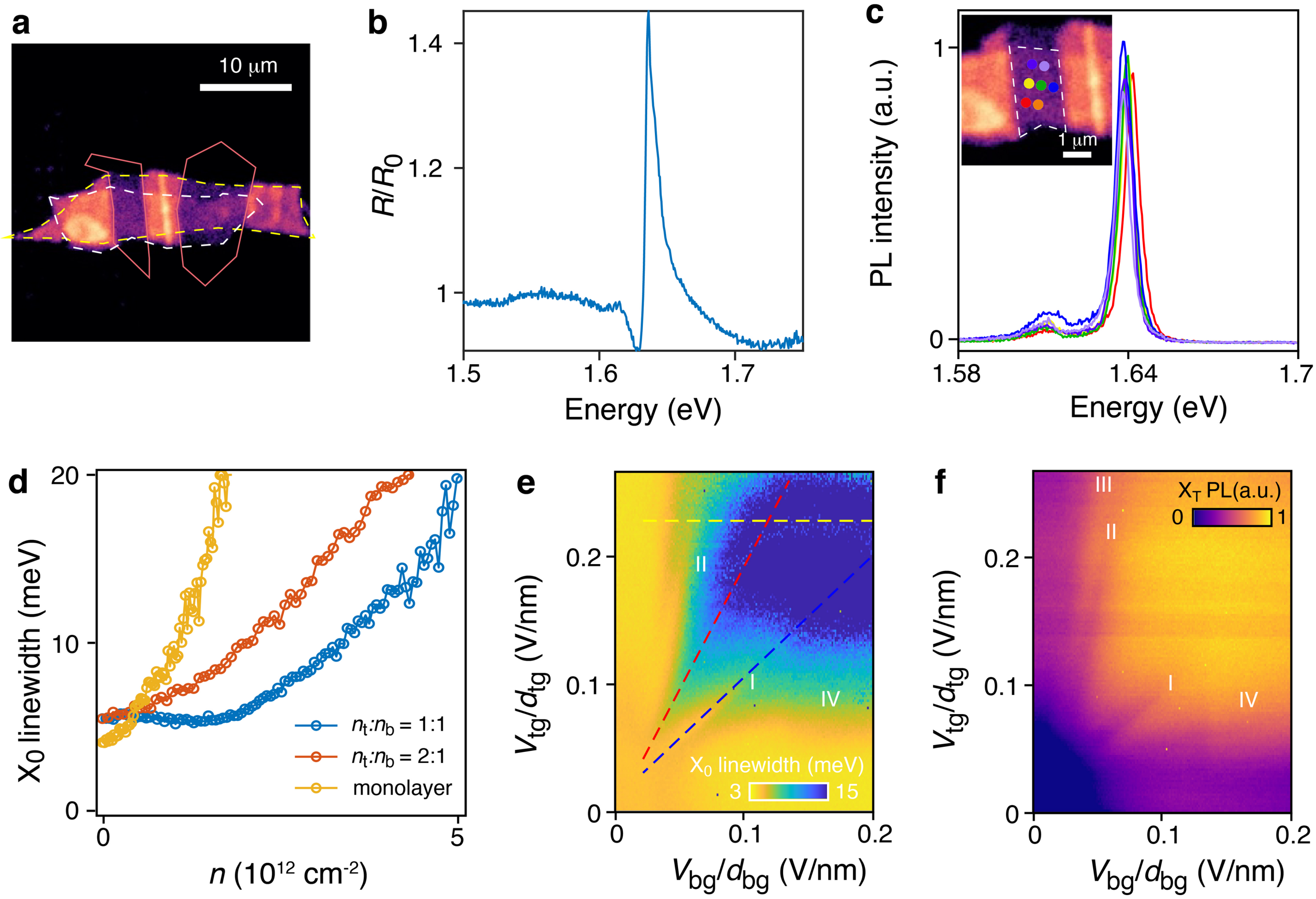

Extended Data Fig. 1 | Optical spectroscopic characterization of device D1 at $T = 4$ K. a, A spatial map of integrated PL intensity at (0 V, 0 V). The PL intensity from the $MoSe_2$/hBN/$MoSe_2$, which is quite uniform throughout the entire region, is stronger than that from the monolayer regions, suggesting that both $MoSe_2$ layers maintain their direct bandgap. **b**, Reflection contrast R/R_0 at (0 V, 0 V). **c**, Representative PL spectra taken from the gated region of device D1 at 4 K. We find the standard deviation of the exciton energy across the gated region to be about 1 meV, much less than the exciton linewidth. The inset shows the spots where the PL spectra were collected, with the colour of the dot and of the spectrum curve matching each other. The dashed line encloses the bilayer region covered by both top and bottom gates. **d**, The linewidth of the neutral exciton X_0 as a function of total electron density n, measured along n_t:n_b = 1:1 and 2:1, compared with a monolayer $MoSe_2$. **e**, 2D maps of X_0 linewidth as a function of V_{tg}/d_{tg} and V_{bg}/d_{bg}. Free charge carriers in $MoSe_2$ can interact with X_0 by introducing additional scattering, which leads to the broadening of X_0 (refs. [20,21]). The features I, II and IV are defined in the same way as in Fig. 2. Along the n_t:n_b = 1:1 and 4:1 features (I and II), we observe narrower X_0 linewidth. This is further corroboration that the system is in insulating states along these density ratios. The blue, red and yellow dashed lines represent the linecuts where we extract data shown in the same colour in **d**. For large V_{tg} and V_{bg} (top right corner of the graph), the intensity of X_0 becomes very weak and therefore the linewidth cannot be reliably extracted. **f**, 2D maps of integrated charged exciton emission (X_T) as a function of V_{tg}/d_{tg} and V_{bg}/d_{bg}. The features I–IV are defined in the same way as in Fig. 2. We observe reduced X_T emission along features I and II (Fig. 2b).

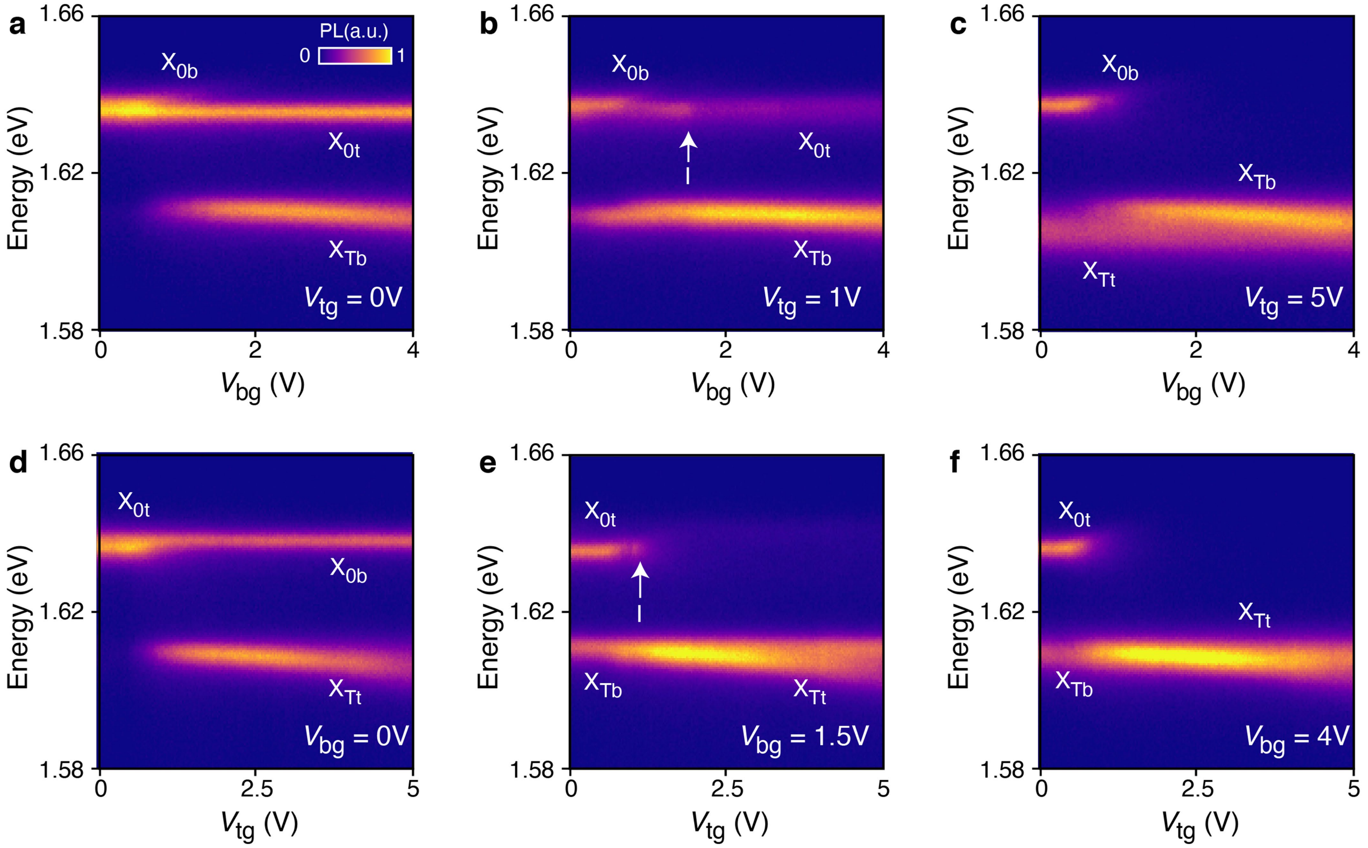

Extended Data Fig. 2 | Gate dependence of PL spectra from device D1 at 4 K. **a**–**c**, PL spectra as a function of V_{bg} with a fixed V_{tg} of 0 V (**a**), 2.5 V (**b**) and 5 V (**c**). **d**–**f**, PL spectra as a function of V_{tg} with a fixed V_{bg} of 0 V (**d**), 1.5 V (**e**) and 4 V (**f**). When the top (bottom) $MoSe_2$ is intrinsic or highly doped, the application of V_{bg} (V_{tg}) mainly modifies the response of the bottom (top) layer. Here X_{0b} and X_{0t} represent the neutral exciton from the bottom and the top layer, respectively, while X_{Tb} and X_{Tt} represent the charged exciton from the bottom and the top layer, respectively. On the basis of such gate dependence, we can distinguish the contributions from the top versus the bottom layer when they have non-degenerate optical response (when the filling ratio is not 1:1). At intermediate gate voltage (**b**, **e**), however, the total PL of the neutral exciton is enhanced at a particular voltage configuration (denoted as I), corresponding to the feature I observed in Fig. 2.

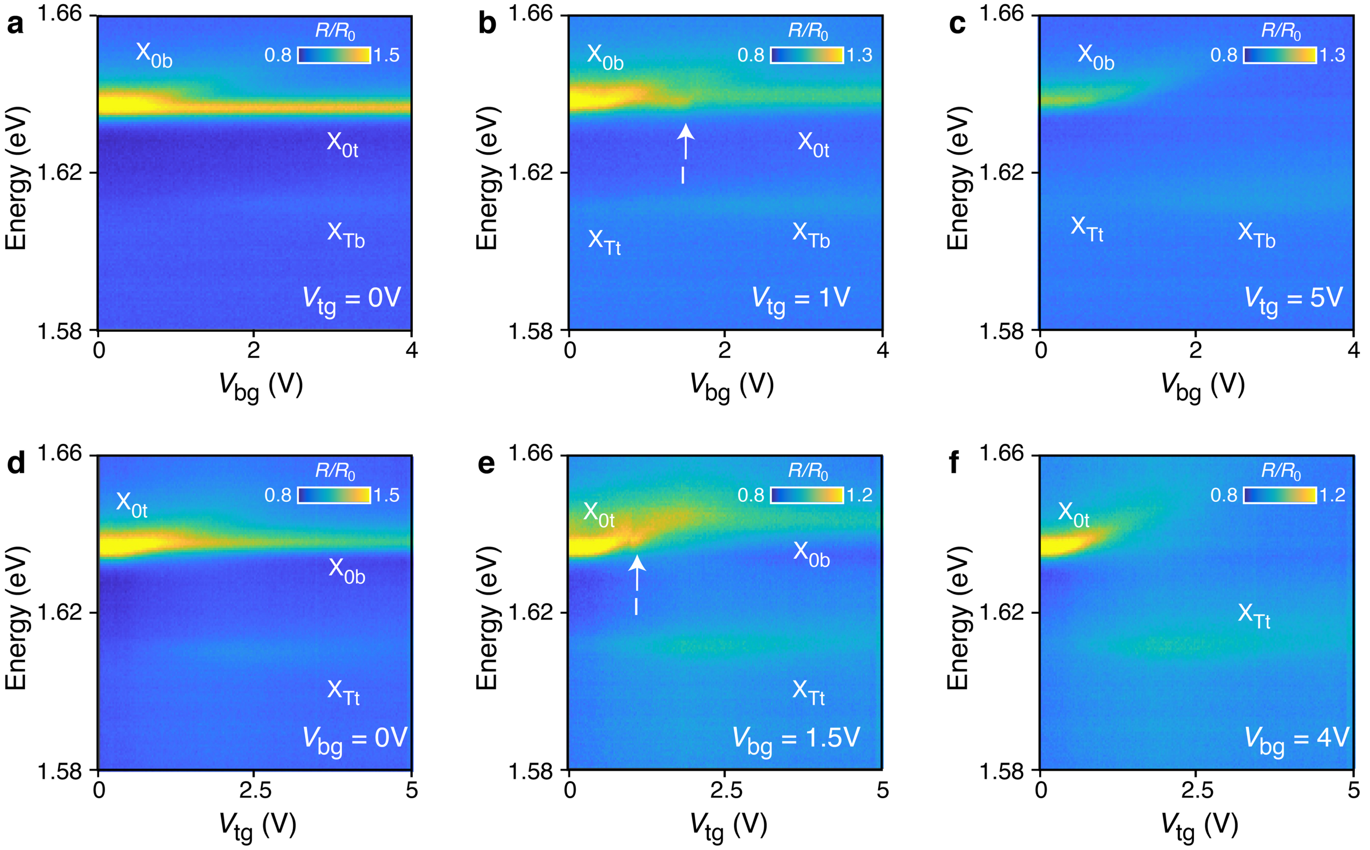

Extended Data Fig. 3 | Gate dependence of reflectance spectra from device D1 at 4 K. a–f, As for Extended Data Fig. 2 but for normalized reflectance, R/R_0; the spectra are normalized to the background reflectance when both MoSe$_2$ layers are highly doped with electrons.

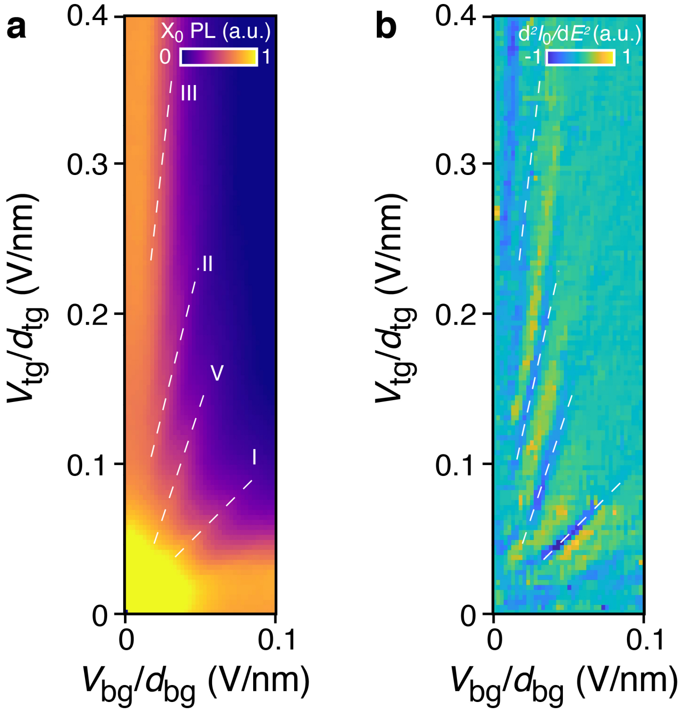

Extended Data Fig. 4 | Optical characterization of device D1 at 100 mK. **a**, **b**, 2D maps of integrated neutral exciton X_0 PL (**a**) and the second derivative of X_0 PL intensity with respect to the electric field (**b**), as a function of V_{tg}/d_{tg} and V_{bg}/d_{bg}. The density ratios can be determined from the troughs in **b**. We added guide lines I, II, III and V, which correspond to constant density ratio n_t:n_b of 1:1, 4:1, 7:1 and 3:1, respectively.

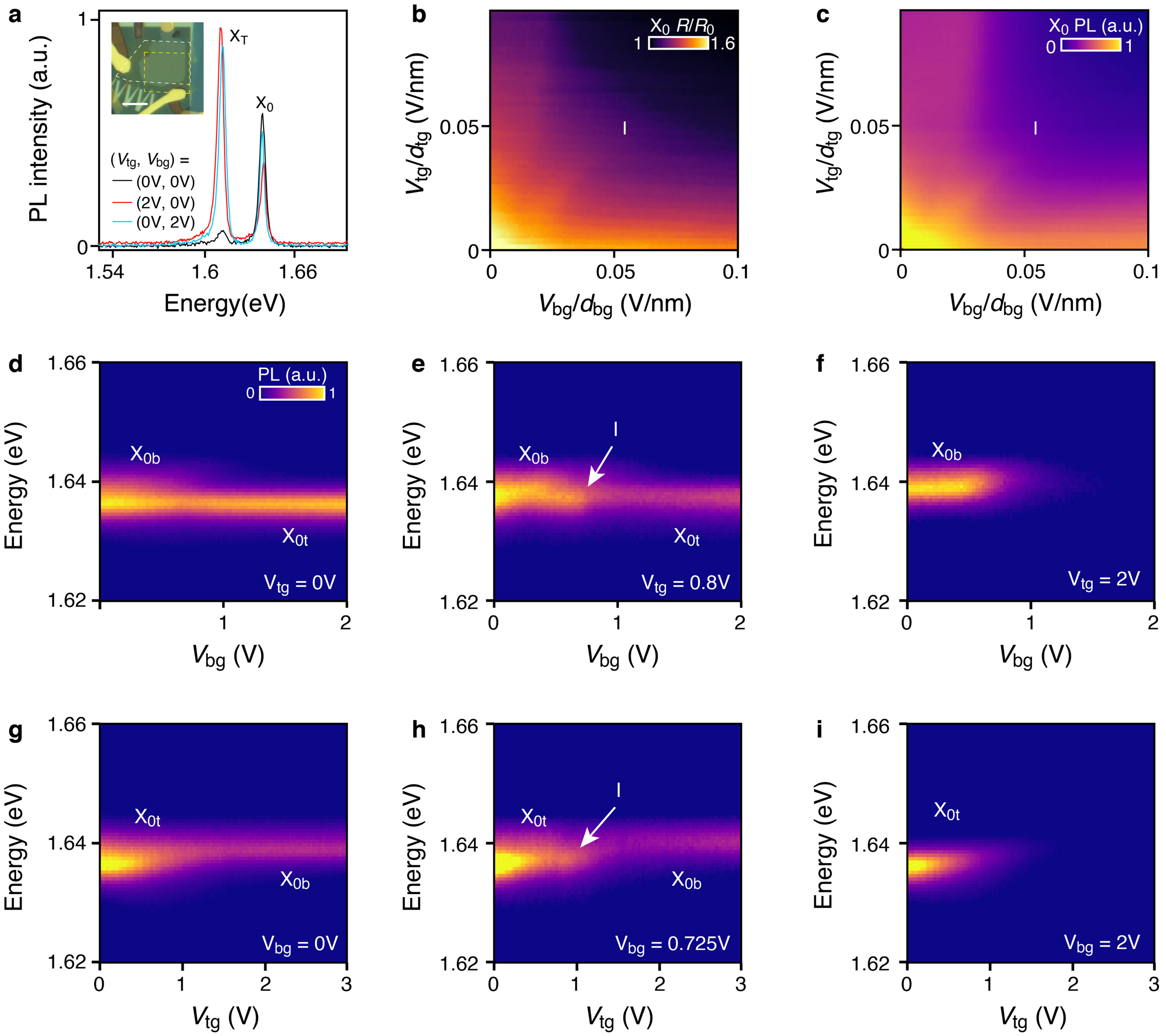

Extended Data Fig. 5 | Observation of bilayer Wigner crystals in another $MoSe_2$/hBN/$MoSe_2$ device, D2, at 4 K. **a**, PL spectrum of D2 at zero gate bias. Inset, a microscope image of D2. In this device, the inter-layer hBN thickness is 1.6 nm. The white and yellow dashed lines indicate top and bottom monolayer $MoSe_2$, respectively. Scale bar, 10 μm. **b**, **c**, 2D maps of neutral exciton X_0 reflectance contrast R/R_0 (**b**) and integrated X_0 PL (**c**), as a function of V_{tg}/d_{tg} and V_{bg}/d_{bg}. The emerging insulating feature I corresponds to a density ratio of n_t:n_b = 1:1, with a lower critical density than found in device D1; we did not observe insulating states at other density ratios. Taken together, this suggests that bilayer Wigner crystals are less stable for this larger inter-layer separation. **d**–**f**, Gate-dependence of PL spectra from device D2 at 4 K with a fixed V_{tg} of 0 V (**d**), 0.8 V (**e**) and 2 V (**f**). **g**–**i**, As **d**–**f** but with a fixed V_{bg} of 0 V (**g**), 0.725 V (**h**) and 2 V (**i**). Such gate-dependent behaviours are similar to those of D1.

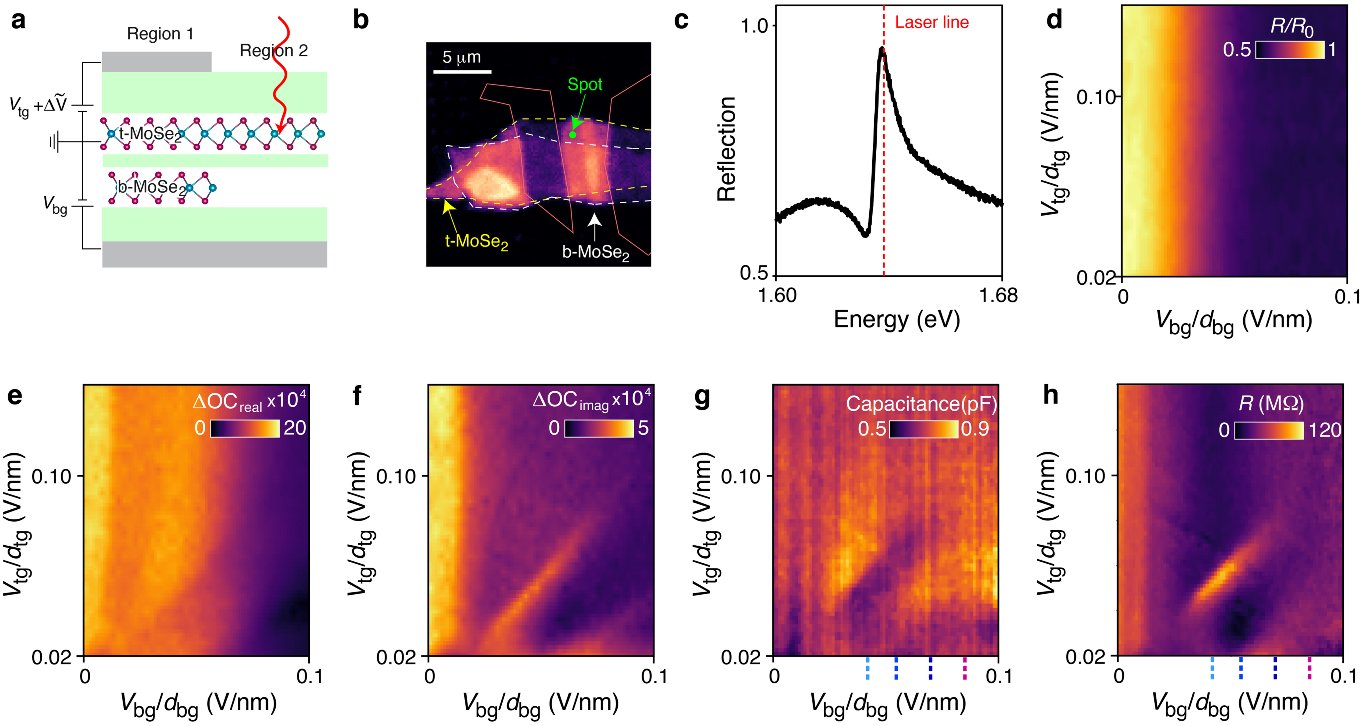

Extended Data Fig. 6 | Optically detected resistance and capacitance measurements of device D1 at 4 K. a, Schematic of the optically detected resistance and capacitance measurements of device D1 with a partial top gate and a global back gate (grey area at top and bottom, respectively). The green layers are hBN dielectrics. A d.c. bias is applied to the top and bottom gates (V_{tg} and V_{bg}, respectively) and a small a.c. bias ($\Delta\tilde{V}$) is superimposed on the top gate voltage. When the frequency of the a.c. voltage is high (typically a few kHz in our experiment), no charge can be injected from the metal contact into MoSe$_2$, but there is charge redistribution between region 1 and region 2. The dynamics of such charge redistribution provide information on the quantum capacitance and resistance of the gated region, which can be probed by the reflectance change of excitons in the ungated region 2 (here we represent the incident probe light using the red arrow). **b**, A spatial map of integrated PL intensity showing the extent of the t-MoSe$_2$ and b-MoSe$_2$ layers as yellow and white dashed lines, respectively. The green circle represents the detection spot. The solid red lines show the outline of the partial top gates. **c**, Reflection spectra from the spot indicated by the green circle in **b** at (0 V, 0 V). The red dashed line represents the continuous wave laser centred at 1.637 eV for probing resistance and capacitance. **d**, A 2D map of neutral exciton reflectance contrast at 1.637 eV as a function of V_{tg}/d_{tg} and V_{bg}/d_{bg}. Reflectance contrast is not affected by the d.c. bias applied to the local top gate, V_{tg}, as expected. **e**, **f**, 2D maps of the reflectance contrast change ΔOC which is in-phase (**e**) and out-of-phase (**f**) with the a.c. modulation voltage. We observe a reduction in the in-phase component X and an increase in the out-of-phase component Y along the 1:1 feature. The magnitude of |ΔOC| is reduced along this feature. **g**, **h**, Extracted capacitance (**g**) and resistance (**h**) of region 1 based on the effective a.c. circuit model and equation presented in Methods. The coloured dashed lines indicate the bottom-gate voltages for the line profiles in Fig. 2d in the main text.

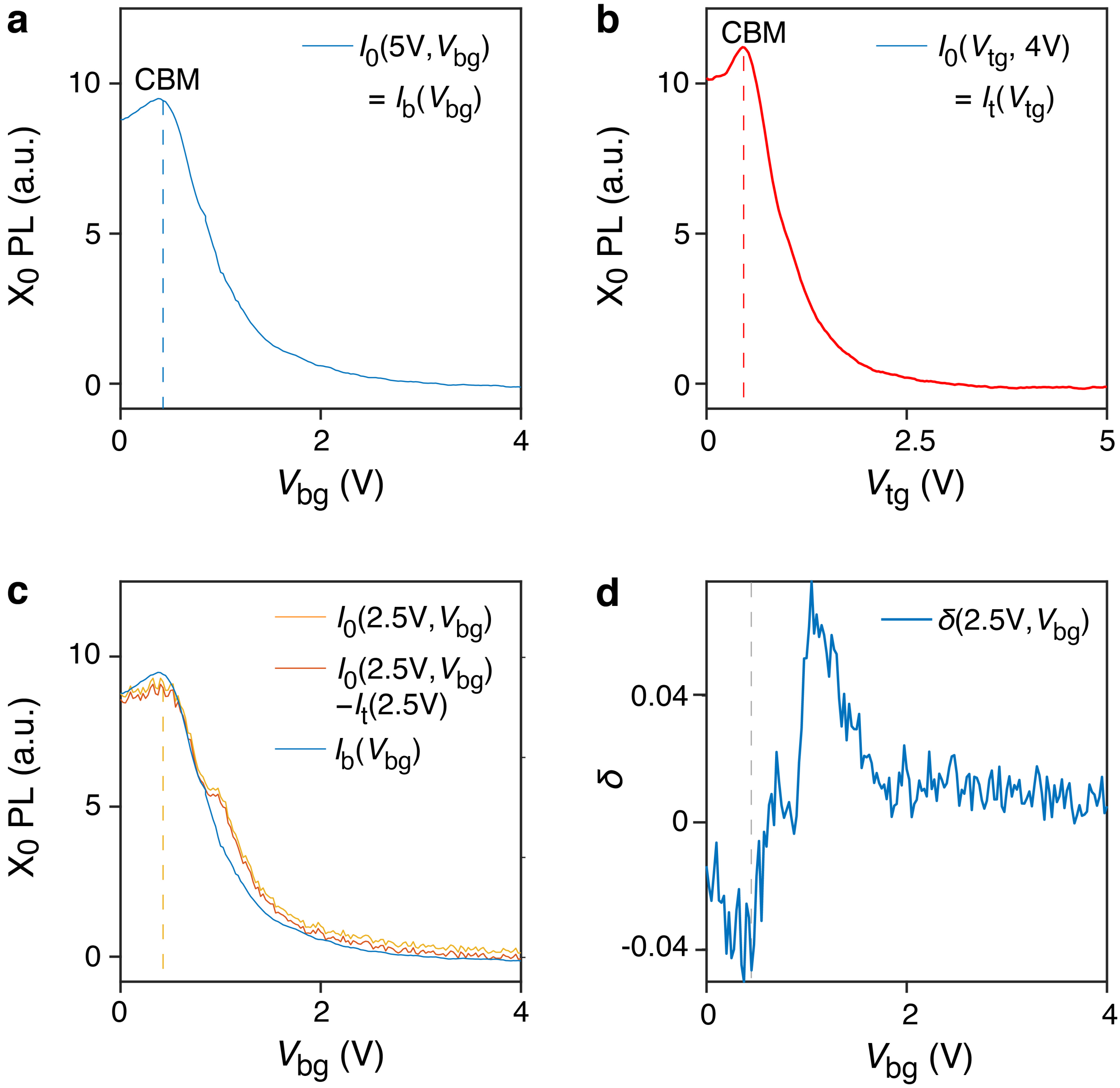

Extended Data Fig. 7 | Examples of procedures for estimating $I_t(n_t)$, $I_b(n_b)$ and δ. **a**, **b**, The integrated PL intensity from X_0, I_0, as a function of V_{bg} (V_{tg}) while keeping V_{tg} (V_{bg}) at a large value. Because the X_0 emission from the heavily doped layer can be omitted, these values can used to estimate $I_t(n_t)$ and $I_b(n_b)$: that is, $I_0(n_t, n_b^+) = I_t(n_t) + I_b(n_b^+) = I_t(n_t)$, and $I_0(n_t^+, n_b) = I_t(n_t^+) + I_b(n_b) = I_b(n_b)$. Here n_t^+ and n_b^+ denote the heavily electron-doped top and bottom layer, respectively. We note the value of I_0 only begins to decrease above a finite gate voltage, which corresponds to the conduction band minimum. On the basis of this, we can estimate the carrier density using ΔV_{tg} (ΔV_{bg}), which is the applied top (bottom) gate voltage relative to the onset voltage corresponding to the conduction band edge. **c**, The value of I_0 as function of V_{bg} while keeping V_{tg} at 2.5 V (yellow curve). To calculate δ, we first subtract $I_t(2.5\,\text{V})$ from the raw I_0 data (red curve). The relative enhancement of the red curve with respect to the $I_b(V_{bg})$ curve (blue) represents the enhancement due to bilayer Wigner crystal formation. **d**, The value of δ at $V_{tg} = 2.5$ V determined using this method. We note that near the band edge δ becomes less than zero because of the $MoSe_2$ layer's weak screening and the difficulties in estimating $I_t(n_t)$ or $I_b(n_b)$ when the layer is intrinsic.

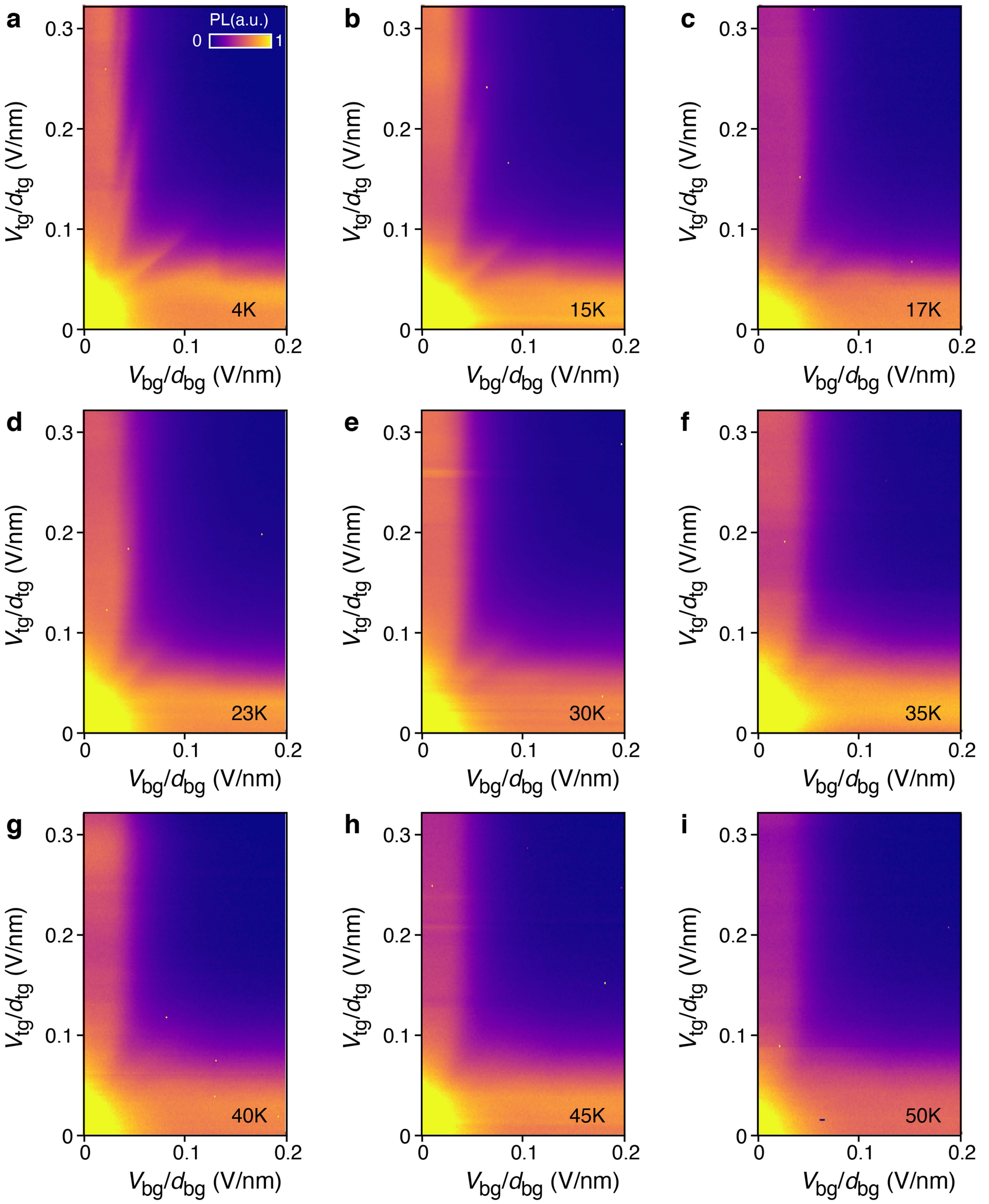

Extended Data Fig. 8 | 2D maps of integrated X_0 PL intensity of device D1 as a function of V_{tg}/d_{tg} and V_{bg}/d_{bg} at various temperatures. a–i, 2D maps measured at temperatures (in K) of 4, 15, 17, 23, 30, 35, 40, 45 and 50, respectively. The insulating features become weaker and broader at higher temperatures and eventually disappear.

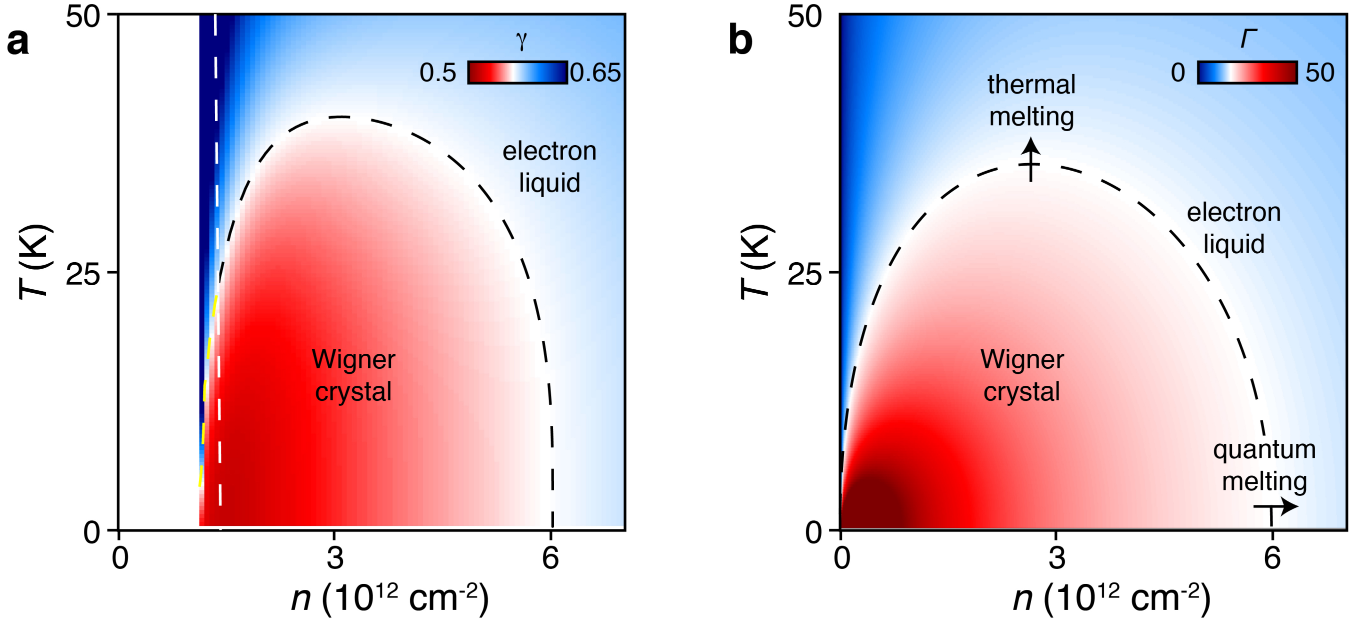

Extended Data Fig. 9 | 2D maps of γ and Γ as a function of total density n and temperature T. **a**, 2D map of Lindemann parameter γ. The dashed black and yellow line represents the contour of $\gamma = 0.56$, the phase boundary between the classical bilayer Wigner crystal and the electron liquid, estimated from the experimentally determined critical density at 4 K (see Supplementary Information for details). The white dashed line represents the density at which theory predicts the staggered triangular lattice structure becomes unstable, giving way to a sequence of structural transitions[34]. **b**, 2D map of Γ, which is the ratio of the average Coulomb energy to the thermally averaged kinetic energy per electron. The black dashed line represents $\Gamma = 17$, also estimated from the experimentally determined critical density at 4 K. The black arrows along the x and y directions indicate respectively thermal melting and quantum melting of the bilayer Wigner crystal. We note that at finite temperatures Γ is not equivalent to the interaction parameter r_s, which is the ratio of the Coulomb energy to the Fermi energy at 0 K (see Supplementary Information).

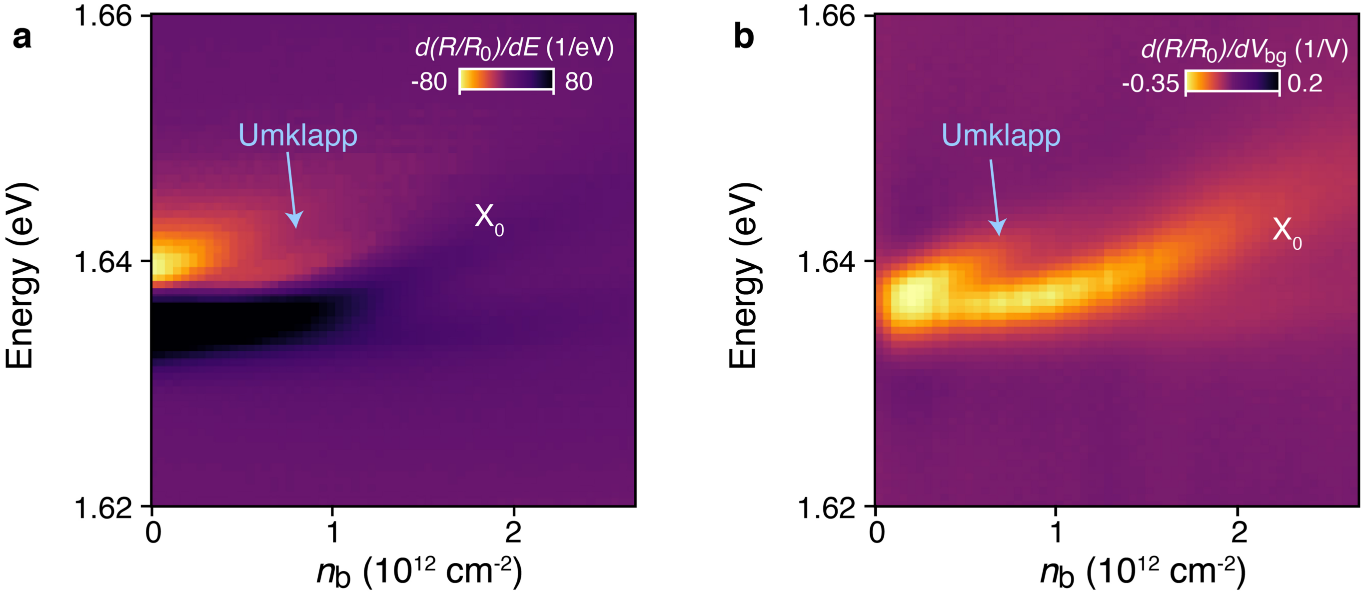

Extended Data Fig. 10 | Umklapp scattering from Wigner crystals measured in device D1 at 4 K. a, The derivative of the reflectance contrast R/R_0 with respect to photon energy E, as a function of bottom-layer carrier density n_b, measured along n_t:n_b = 1 in device D1 at 4 K. In addition to the neutral exciton X_0, an umklapp scattering peak may be seen, whose energy shifts linearly with carrier density. **b**, To further enhance the contrast of the features, we take the derivative of the reflectance contrast R/R_0 with respect to V_{bg}; this clearly shows the evolution of both exciton X_0 and its umklapp scattering. In the weak coupling regime, the exciton scattering will probably be dominated by the electrons from the same layer. In addition, for a bilayer Wigner crystal with the same density in each layer, the primitive unit cell is the same as that of each individual layer. On the basis of these considerations, we can estimate the exciton mass from the density dependence of the splitting between X_0 and the umklapp peak. We estimate the exciton mass to be about 1.8m_e, which is in agreement with literature[22], given the uncertainties in determining the slope of the energy shift and electron densities.